Ultrafast Response of a Hybrid Device Based on Strongly Coupled Monolayer WS_2 and Photonic Crystals: The Effect of Photoinduced Coulombic Screening

Yuxiang Tang, Yanbin Zhang, Hao Ouyang, Maoxiong Zhao, Hao Hao, Ke Wei, Han Li, Yizhen Sui, Jie You, Xin Zheng, Zhongjie Xu, Xiangai Cheng, Lei Shi, and Tian Jiang**

Quantum interactions between transition metal dichalcogenides (TMDs) and optical cavities are rapidly becoming an appealing research topic since these interactions underly a broad spectrum of optical phenomena. Here, we fabricate a simple device in which coherent strong coupling interactions occur between a photonic crystal (PhC) slab and monolayer tungsten disulfide (WS_2). Both steady-state angle-resolved spectroscopy and transient absorption microscopy (TAM) are employed to explore the coupling behavior of this device. Specifically, anticrossing dispersions are observed in the hybrid device, indicating a Rabi splitting of 40.2 meV. A newly formed spectral feature emerges in the transient absorption (TA) spectrum of this polariton device under near-resonant excitation, which is subsequently evidenced to be a signature of the upper hybrid exciton–polariton state. Moreover, by carefully analyzing the ultrafast responses of both bare WS_2 and the WS_2-PhC polariton device excited both off resonance and near resonance, it is found that nonequilibrium thermal decay induces Coulombic screening in the monolayer WS_2, which has a major impact on the formation of exciton–polariton. The results of this work could not only improve the current understanding of photophysics in the strong light–matter coupling regime but also lay the foundation for tailoring the development of TMD-based coherent devices.

1. Introduction

The control of light–matter interactions at the nanoscopic scale is fundamental to many contemporary scientific disciplines.[1–6] Among the related research fields in which new interest has arisen, the study of the interactions between quantum emitters and optical cavities in particular is driving considerable research activity.[7–14] These interactions fall into two distinct regimes, referred to as weak and strong coupling. In the weak coupling regime, the eigenstates of a coupled system remain unchanged relative to their initial uncoupled states, and the presence of cavities merely modifies the spontaneous emission rate due to the corresponding changes in the local density of photonic states, in a phenomenon referred to as the Purcell effect.[15–18] However, when the rate of the coherent energy oscillations between the two components becomes even faster than their respective dissipation rates, new hybrid quasi-particles known as polaritons[19–21] are formed, and hence, the regime of strong coupling is reached.[22–30] In this regime, the cavity electromagnetic modes and matter wavefunctions exist in a coherent superposition, and the hybridization as a whole manifests itself as two characteristic polaritonic states, in which the phenomenon of Rabi splitting[31] is observed. Apart from their fundamental importance in research on cavity quantum electrodynamics, the coherent coupling effects between light and matter not only feature a plethora of rich physics phenomena, such as Bose–Einstein

Y. Tang, H. Ouyang, K. Wei, H. Li, Y. Sui, Prof. Z. Xu, Prof. X. Cheng, Prof. T. Jiang
College of Advanced Interdisciplinary Studies
National University of Defense Technology
Changsha 410073, P. R. China
E-mail: tjiang@nudt.edu.cn

Y. Zhang, M. Zhao, Prof. L. Shi
Key Laboratory of Micro- and Nano-Photonic Structures (Ministry of Education), and State Key Laboratory of Surface Physics
Department of Physics
Fudan University
Shanghai 200433, P. R. China
E-mail: lshi@fudan.edu.cn

H. Hao
State Key Laboratory of High Performance Computing
College of Computer
National University of Defense Technology
Changsha 410073, P. R. China

Dr. J. You, Prof. X. Zheng
National Institute of Defense Technology Innovation
Academy of Military Sciences PLA China
Beijing 100010, P. R. China

The ORCID identification number(s) for the author(s) of this article can be found under https://doi.org/10.1002/lpor.201900419

DOI: 10.1002/lpor.201900419

condensation,[32] enhanced carrier mobility,[33–35] and long-range energy transfer,[36] but also serve to enable many practical functionalities, including optical switching,[37] low-threshold polariton lasing,[38–42] and quantum information processing.[43]

Recently, newly emerging atomically thin transition metal dichalcogenides (TMDs) have received considerable critical attention since they possess a pronounced exciton oscillator strength (i.e., high transition dipole moments) with a large binding energy[44–47] and a distinct valley degree of freedom.[48–54] These exceptional properties make TMDs suitable candidates for application in the strong coupling regime[55] compared with other material systems.[22,40,56–58] To date, strong coupling has been widely observed in various hybrid photonic devices consisting of TMDs and optical cavities of various shapes, including Fabry–Pérot (FP) cavities or distributed Bragg reflectors,[59,60] metallic nanoparticles,[61–66] and plasmonic arrays,[67–72] accompanied by alternative fascinating phenomena such as valley-polarized exciton–polaritons[28,73–76] as well as polariton light-emitting diodes.[77] Benefiting from the delocalized nature of their Bloch modes and their designable properties, photonic crystals (PhCs) are becoming an important platform for approaching the strong exciton–photon coupling regime with TMDs,[78] an approach that is regarded as flexible, practical, and ultracompact in on-chip science.

The corresponding rapid technological developments and attractive application scenarios for strongly coupled photonic devices are creating an increasing demand for a thorough understanding of the photophysical processes occurring in TMD-based polariton devices. However, thus far, little research has been devoted to investigating the underlying mechanism governing strong light–matter coupling.[79] In particular, the ultrafast response of TMD-based polariton devices after photoexcitation is not yet well understood. Recent studies[80,81] have documented the ability of equilibrium charge carriers injected into TMDs by applied external fields to switch devices from the strong coupling regime to the weak coupling regime due to the efficient screening of Coulomb interactions. In fact, in addition to the static modification of Coulomb interactions that can be introduced in TMDs,[82,83] the Coulomb interactions in TMDs can also undergo a transient modification after the absorption of light.[84–86] This phenomenon raises a key question: how can these nonequilibrium changes in Coulombic screening in TMDs affect the ultrafast response of a strongly coupled hybrid device? It is of critical importance to investigate the transient dynamics of TMD-based polariton devices after optical excitation and obtain an in-depth understanding of how the Coulombic screening phenomenon can be exploited to influence the strong coupling effect, since such investigations will not only contribute to the understanding of the fundamental photophysical nature of hybrid light–matter states but also provide a fertile platform for the design and optimization of a new class of coherent nanodevices, which might permit the tunability of light–matter interactions.

In this work, we demonstrate coherent strong coupling at room temperature between the excitons in monolayer (ML) WS_2 and the guided Bloch modes in a PhC slab consisting of a passivated silver substrate covered with a periodically textured polymethyl methacrylate (PMMA) thin film. By means of angle-resolved reflectance and photoluminescence (PL) spectroscopy, the dispersions of this hybrid WS_2-PhC device are measured and found to show anticrossing behavior, revealing a Rabi splitting of 40.2 meV. Furthermore, by means of systematic ultrafast pump–probe measurements, a new spectral feature in the TA spectrum is clearly shown, which is then experimentally confirmed to correspond to the upper polariton band. More importantly, the dynamics of the hybrid WS_2-PhC device and of bare WS_2 under different excitation wavelengths, from off-resonance to near-resonance wavelengths, are carefully investigated and compared, showing that nonequilibrium dipolar screening changes in ML WS_2 under nonresonant photoexcitation can strongly alter the formation of exciton–polaritons. The findings concerning the ultrafast response of the WS_2-PhC polariton device, especially the effect of nonequilibrium photoinduced Coulombic screening on strong coupling as indicated by this work, are expected to deepen the understanding of the inherent polaritonic physics and provide guidance toward the design and realization of novel coherent devices.

2. Sample Preparation and Characterization

The fabrication procedure for the hybrid WS_2-PhC device is illustrated in Figure S1, Supporting Information. First, a precleaned silicon substrate was prepared, and a 200-nm-thick flat silver film was deposited on the substrate using a thermal evaporator. Then, the silver film was passivated with 15-nm-thick atomic-layer-deposited Al_2O_3 to protect it from degradation and avoid short-range interactions[87,88] (i.e., charge transfer) between the 2D semiconductor and the silver. Subsequently, ML WS_2, which had been synthesized via chemical vapor deposition methods, was transferred onto this nonconductive silver substrate using wet transfer technique. Afterward, a 150-nm-thick layer of PMMA was spin coated onto the passivated silver film covered with ML WS_2. Finally, the PMMA layer was partially etched by means of electron-beam lithography to form a 1D grating. The resulting 1D PMMA grating together with the remaining bottom PMMA slab support a certain desired Bloch resonance, which can be tuned to oscillate with the excitons in the ML WS_2.

A schematic illustration of the WS_2-PhC device is shown in **Figure 1**a. Notably, the ML WS_2 is sandwiched between the 1D grating-etched PMMA thin film (acting as the superstrate) and the passivated silver mirror (acting as the substrate). From the scanning electron microscopy (SEM) and atomic force microscopy (AFM) images shown in Figure 1b,c, respectively, a good 1D grating morphology is observed, we can confirm the successful preparation of our hybrid WS_2-PhC device. In addition, several device parameters can be extracted from Figure S2, Supporting Information: the total thickness of the PMMA is $t \approx 150 \pm 10$ nm, and the period, height, and width of the grating are $p \approx 480 \pm 10$ nm, $h \approx 50 \pm 10$ nm, and $w \approx 300 \pm 20$ nm, respectively. In addition, the Raman spectrum of the active medium WS_2 is shown in Figure 1d. After peak fitting, we can observe that the peak shift from the $A^1{}_g$ (out-of-plane vibration) mode to the $E^1{}_{2g}$ (in-plane vibration) mode is 60.66 cm^{-1}, which is consistent with previous reports for ML WS_2.[89] Moreover, we compare the PL spectra and PL mapping images for the bare WS_2 area and the hybrid WS_2-PhC device, as shown in Figure 1e and Figure S3, Supporting Information, respectively. The PL intensity (the intensity of the peak located at ≈612.0

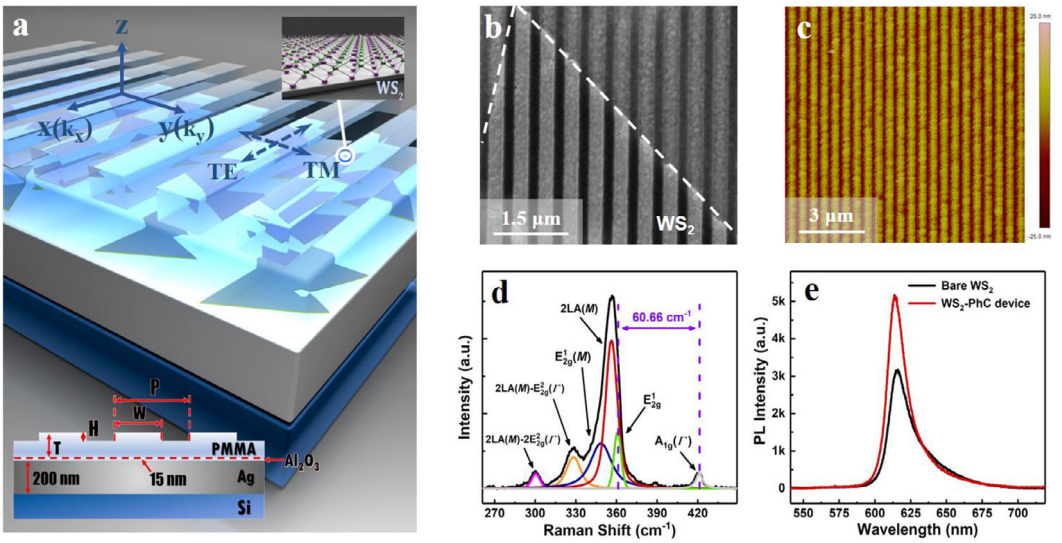

Figure 1. Schematic illustration and characterization of the hybrid WS_2-PhC device. a) Cartoon illustration of the hybrid WS_2-PhC device. Notably, the ML WS_2 is sandwiched between a 1D periodically textured PMMA thin film and a passivated silver substrate. The structure parameters of the PhC are as follows: total PMMA thickness $t \approx 150 \pm 10$ nm, grating height $h \approx 50 \pm 10$ nm, period $p \approx 480 \pm 10$ nm, and grating width $w \approx 300 \pm 20$ nm. Inset: a side view of the device. b) SEM image of the hybrid WS_2-PhC device (a WS_2 flake is outlined with a dashed white line). The scale bar represents 1.5 μm. c) AFM image of the hybrid WS_2-PhC device. The scale bar represents 3 μm. d) Raman spectrum of the ML WS_2, where the Raman peaks are fitted with Lorentz line shapes. e) PL spectra of the bare WS_2 area and the hybrid WS_2-PhC device under 532 nm continuous laser excitation.

nm) is significantly enhanced in the WS_2-PhC device relative to the bare WS_2 area, which may be due to the change in the local density of photonic states, thus validating the existence of coupling interactions between the ML WS_2 and the PhC. The relevant coupling strength of the interactions between the ML WS_2 and the PhC will be discussed in the following section.

3. Results and Discussion

3.1. Steady-State Measurements of the WS2-PhC Polariton Device

To gain further insight into the coupling effect in the hybrid WS_2-PhC device, the measured angle-resolved white-light reflectance spectra of the sample are analyzed, as shown in **Figure 2**. Considering that the optical modes of the PhC slab are strongly dependent on the propagation and polarization directions of the light field in our angle-resolved experiments, the orientation of the 1D grating structure is always fixed by aligning its cross-bar direction (y-direction) horizontal to the slit of the spectrometer. Additionally, the transverse electric (TE) and transverse magnetic (TM) modes are defined as the cases in which the polarization of the reflected light is parallel to (along) and perpendicular to (across) the cross-bar direction, respectively. Accordingly, the measured wavelength–angle dispersions of the hybrid WS_2-PhC device are presented in Figure 2a for the case of the k_y propagation direction with TE polarization. One can see from this figure that the linear progressive dispersions of the guided Bloch modes through the A excitonic transition are accompanied by obvious anticrossing behavior at ±12.5°. For greater precision, the reflectance spectra corresponding to incidence angles varying from $\theta = 8°$ to $\theta = 17.6°$ in increments of 0.6°, as extracted from the corresponding wavelength–angle dispersion image in Figure 2a, are plotted in Figure 2b. It is apparent that the linear guided mode dispersion splits into two parts, which are referred to as the upper and lower polariton (UP and LP) bands, as represented by the dark red dashed lines. In addition, the results of measuring the angle-resolved PL spectrum of the WS_2-PhC polariton device are presented in Figure S4, Supporting Information, where the same anticrossing behavior is observed. These unambiguous anticrossing behaviors in the angle-resolved spectroscopy results suggest that the hybrid WS_2-PhC device operates in the strong coupling regime. To further confirm the formation of a hybrid light–matter state, we plot the minima of the reflectance spectra in Figure 2c and fit these data using two coupled oscillator model with a Hamiltonian that is mathematically expressed as

$$H = \begin{bmatrix} E_{\mathrm{PhC}}(\theta) - i\frac{\gamma_{\mathrm{PhC}}}{2} & g \\ g & E_{\mathrm{exc}} - i\frac{\gamma_{\mathrm{exc}}}{2} \end{bmatrix} \quad (1)$$

where E_{PhC} and E_{exc} represent the energy of the bare PhC and the A excitons in the bare ML WS_2, respectively; γ_{PhC} (20 meV) and γ_{exc} (36 meV) are the linewidths (full-width at half-maximum, FWHM) of the bare PhC resonances and uncoupled A excitons, respectively, which correspond to the dissipation rates of the guided Bloch modes and excitons; and g is the coherent exciton–photon coupling strength. By diagonalizing the Hamiltonian matrix, we can obtain the solution for the two eigenenergies of the polariton modes, $E_{\mathrm{UP,LP}}$, as given below.

$$E_{\mathrm{UP,LP}} = \frac{1}{2}\left[E_{\mathrm{PhC}}(\theta) + E_{\mathrm{exc}} + i\left(\gamma_{\mathrm{PhC}}/2 + \gamma_{\mathrm{exc}}/2\right)/2\right] \pm \sqrt{g^2 + \frac{1}{4}\left[E_{\mathrm{exc}} - E_{\mathrm{PhC}}(\theta) + i\left(\gamma_{\mathrm{PhC}}/2 - \gamma_{\mathrm{exc}}/2\right)\right]^2} \quad (2)$$

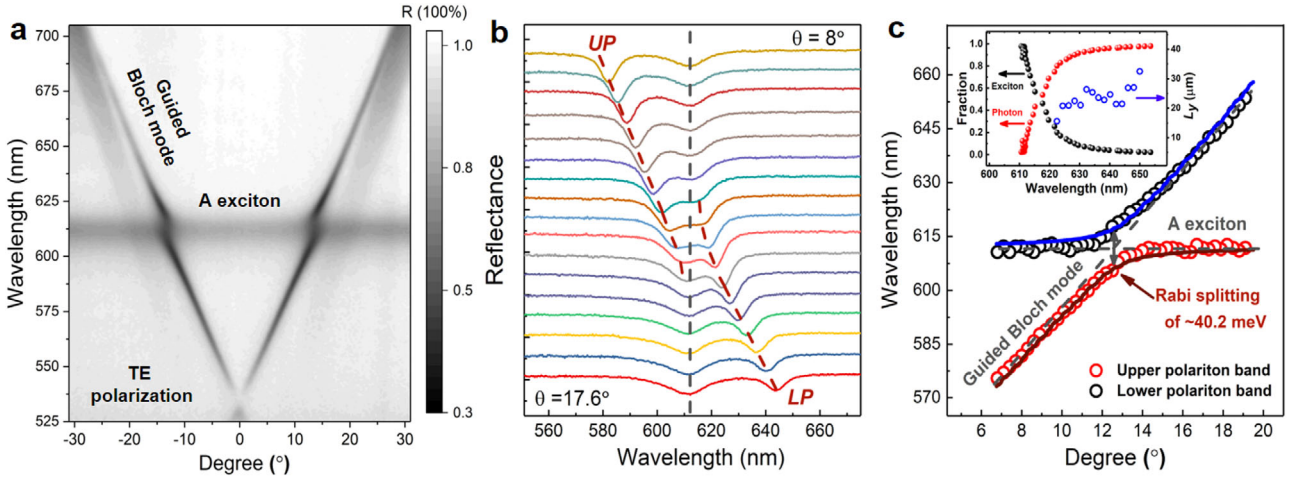

Figure 2. Strong coupling between ML WS_2 excitons and guided Bloch modes measured in the k_y propagation direction with TE polarization at room temperature. a) The measured wavelength–angle dispersion for the PhC with ML WS_2, showing clear anticrossing behavior at ±12.5°. The exciton and guided Bloch mode dispersions are labeled in the figure. b) Reflectance spectra at various probe angles (θ from 8° to 17.6°, in increments of 0.6°), representing profiles cutting through the corresponding dispersion image in (a). The black dashed line represents the A excitonic transition energy of the bare ML WS_2, and the red dashed curves represent the splitting of the UP and LP bands. c) Wavelengths corresponding to the minima in the reflectance spectra as a function of the reflection angle for the same device. The upper and lower bands have been fitted using coupled oscillator model (the red and blue solid lines represent the fitting results), yielding a Rabi splitting of 40.2 meV. Inset: the corresponding fractions of photons (red) and excitons (black) as well as the spatial coherence lengths of the hybrid polaritons in the LP bands.

Furthermore, the value of the Rabi splitting, Ω_R, at the resonance condition of $E_{exc} = E_{PhC}(\theta)$ is given by

$$\Omega_R = E_{UP} - E_{LP} = \sqrt{4g^2 - \left(\gamma_{PhC}/2 - \gamma_{exc}/2\right)^2} \quad (3)$$

When the positions of the minima in the reflectance spectra are fitted with Equations (2) and (3), as shown in Figure 2c, the fitted curves (i.e., the blue and red lines) show good consistency with the experimental data. Additionally, a Rabi splitting of 40.2 meV is extracted here. To support the claim of strong exciton–photon coupling, we can evaluate whether the strict criterion for strong coupling is satisfied by using the parameters (Ω_R, γ_{PhC}, and γ_{exc}) obtained as described above. In the case of strong coupling, $\Omega_R^2 > (\gamma_{PhC}^2 + \gamma_{exc}^2)/2$ or $\Omega_R > (\gamma_{PhC} + \gamma_{exc})/2$ needs to be satisfied.[8,9] In this case, the Rabi splitting energy should be greater than the average decoherence rate of the bare oscillators to guarantee spectral separation of the two newly formed polariton bands. Obviously, this strict criterion is satisfied for our device, thus confirming that our device is operating well within the strong coupling regime. Meanwhile, in the inset of Figure 2c, we show the large spatial coherence length of our polariton modes, calculated as $\lambda/\Delta\theta$,[24] where $\Delta\theta$ is obtained as the FWHM of constant-energy profiles projected from the angle-resolved spectrum. It is suggested that due to the delocalized nature of the guided Bloch modes, the hybridization happens in a large area and the spatial coherence length is as long as 15.5 µm with a 20% exciton fraction, indicating the coherent properties of hybrid polaritons (double slits experiments were also performed to demonstrate the large spatial coherence length of our polariton device in Figure S5, Supporting Information). To verify the accuracy of our experimental tests, we also simulated the angle-resolved reflectance spectra of our hybrid device using the transfer matrix method, as shown in Figure S6, Supporting Information. Not surprisingly, the simulated configuration agrees well with the experimental results presented above. To conclude, all of these experimental and simulated results firmly place the interactions of our device within the strong coupling regime, thus demonstrating the feasibility of further investigation into strong coupling phenomena.

3.2. Transient Dynamics of the WS2-PhC Polariton Device

Although the aforementioned steady-state measurements confirm the existence of strongly coupled hybrid states, the present static approaches face considerable challenges in providing greater insight into the photophysics of these hybrid light–matter states, especially from a transient temporal perspective. A key related issue, which has yet to be investigated in the literature, is the ultrafast response of a strongly coupled TMD-based polariton device after photoexcitation. Inspired by Wang's work,[90] transient absorption microscopy (TAM) experiments performed under both off-resonant and near-resonant conditions are reported here to elucidate the complex behavior of the hybrid exciton–polariton states in this composite photonic device. Specifically, for broadband TAM in a setup with a reflection geometry,[91,92] a femtosecond pulse from a Ti-sapphire laser (≈100 fs, 800 nm, 1 kHz) was divided into two different beams. The stronger beam was sent to an optical parametric amplifier (TOPAS, Coherent) to generate tunable excitation pulses, and the other was focused onto a sapphire crystal to generate a white-light continuum beam to serve as the probe beam. Finally, the changes in optical density (ΔOD) of the probe beam, considering the cases of both pump excitation and no pump excitation, were

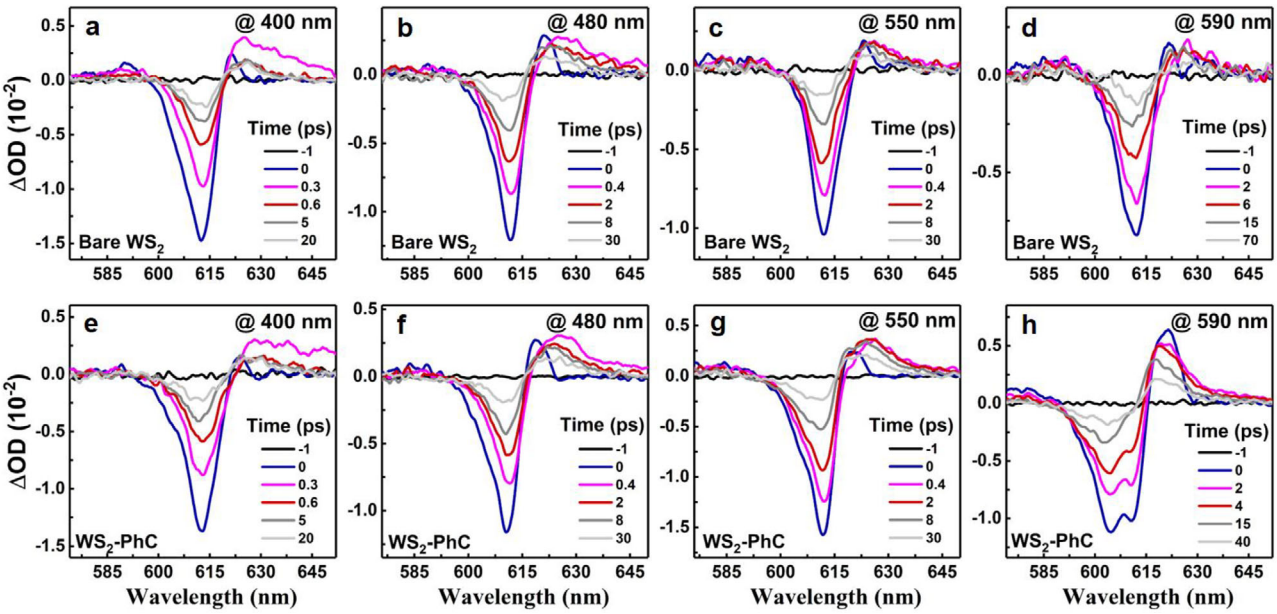

Figure 3. TAM experiments at various excitation wavelengths: bare WS_2 area pumped with a) 400 nm, b) 480 nm, c) 550 nm, and d) 590 nm laser pulse and WS_2-PhC polariton device pumped with e) 400 nm, f) 480 nm, g) 550 nm, and h) 590 nm laser pulse. Notably, all the pump fluences were kept below 10 μJ cm^{-2} and artificially controlled to maintain the ground-state bleaching amplitude measured at 2 ps (after exciton formation) at a constant value, thus guaranteeing almost the same exciton populations in the device under different excitation wavelengths (the time delay of 0 ps is defined as the time at which the pump pulse and probe pulse are almost temporally overlapped, where the absolute signal value reaches a maximum).

recorded following a series of time delays. Further details about the experimental setup are provided in the experimental section.

Thus, a series of TAM experiments were conducted at different excitation wavelengths for both bare WS_2 area and the WS_2-PhC polariton device. For illustration, the typical TA spectra of the bare ML WS_2 under four excitation wavelengths (i.e., 400, 480, 550, and 590 nm) are presented in **Figure 3**a–d. In all cases, these TA spectra are dominated by the ground-state bleaching signal at the A excitonic transition energy, which is often interpreted as reduced absorption due to the band-filling effect of band-edge excitons.[93,94] In addition, a small, broad photoinduced absorption band located on the red side of the optical bandgap is observed in the TA spectra, which is commonly attributed to the intervalley optical Stark effect.[95] By contrast, for the case of the WS_2-PhC polariton device, the TA spectra in Figure 3e–h are characterized by completely different transient behavior. Specifically, from Figure 3e–g, one can see that the TA behaviors of the WS_2-PhC polariton device excited off resonance (at 400, 480, and 550 nm) remain almost unchanged, similar to those of the bare ML WS_2. However, under near-resonant excitation (at 590 nm), as shown in Figure 3h, a newly formed spectral feature emerges at the wavelength of 605.3 nm, where strong coupling occurs. Given these intriguing phenomena, two fundamental questions arise here. 1) What is the nature of the new TA spectral feature of the WS_2-PhC device that emerges under 590 nm excitation, and is it related to the exciton–polariton state? 2) Why can it be detected only under near-resonant conditions?

To answer the first question, the TA spectra of both the bare WS_2 and the WS_2-PhC polariton device were extracted at 0 ps under 590 nm excitation and carefully analyzed; the results are presented in **Figure 4**a. One significant conclusion is that a new TA peak and extensive broadening of the excitonic resonance are observed in the strongly coupled WS_2-PhC device (red line) compared with the single ground-state bleaching signal in the bare WS_2 area (black line). More specifically, the two peaks for the WS_2-PhC polariton device are located at ≈611.4 and 605.3 nm. The first peak corresponds to the uncoupled A excitonic resonance, just like the peak in the bare ML WS_2, whereas the other peak matches well with the position of the UP state (E_{UP}) at resonance, $E_{exc} = E_{PhC}(\theta)$. To confirm whether this intriguing spectral feature originates from the UP state, we first carried out power-dependent TAM experiments on the WS_2-PhC polariton device under 590 nm excitation, as illustrated in Figure 4b. Notably, this new spectral feature exists across a broad range of excitation fluences, excluding the influence of many-body complexes in the ML WS_2.[96] Moreover, the evolution of the peak ΔOD signal with different pump fluences, as shown in the inset of Figure 4c, exhibits linear behavior. And another finding from Figure 4c is that the dynamics of the new peak (at 605.3 nm) are independent of the pump fluence. These consistent observations explicitly place our device in a linear region, indicating nonlinear effects[97,98] will not be responsible for emergence of this new peak. Furthermore, from the TA spectra of the bare PhC presented in Figure S7, Supporting Information, it is found that the bare PhC contribute no TA signal, revealing that this newly formed spectral feature does not originate from the bare PhC. The tests described above show that this new feature is neither derived from the bare ML WS_2 or bare PhC, indicating that the new feature is most probably to be originated from the interactions between the ML WS_2 and PhC. Therefore, we prepared another WS_2-PhC device operating in the intermediate coupling regime (by adjusting the grating height of the PhC), for which a Rabi splitting of 30.9 meV

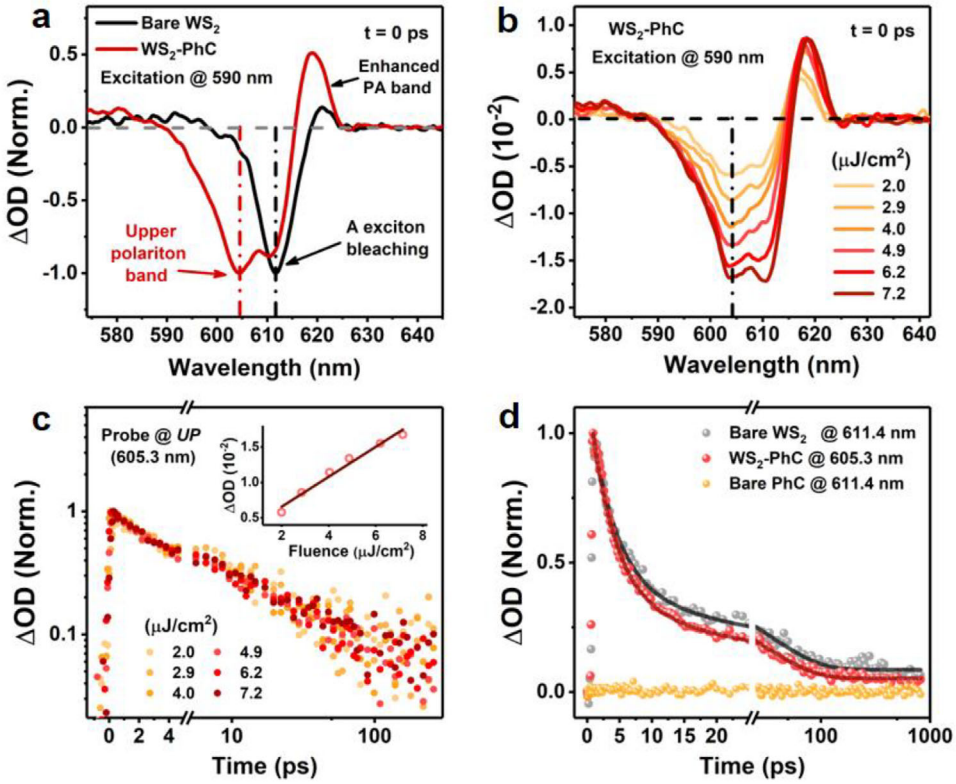

Figure 4. a) Comparison of the TA spectra recorded at a time delay of 0 ps for the bare WS_2 and the WS_2-PhC polariton device. b) TA spectra of the WS_2-PhC polariton device recorded at 0 ps under different excitation fluences. c) Dynamics of the UP band under different excitation fluences. Inset: excitation fluence dependence of the ΔOD signal in the UP band; the red line is a linear fit to the amplitude of the peak ΔOD signal. d) Comparison of the dynamics of the UP band (red) in the WS_2-PhC polariton device and the uncoupled exciton state (gray) in the bare ML WS_2. The solid lines are exponential fits to the data. The ultrafast response of the bare PhC (yellow) is also presented. All measurements were performed under near-resonant excitation (590 nm) at room temperature.

was found on the basis of the angle-resolved reflectance measurements presented in Figure S8a–c, Supporting Information. Then, a subsequent TAM experiment was conducted on this intermediately coupled device under 590 nm excitation, as shown in Figure S8d, Supporting Information. As expected, the TA spectrum of this intermediately coupled WS_2-PhC device also shows the new spectral feature (or shoulder) at short wavelength direction. But, the magnitude of this new peak is comparatively weaker than the one in the strongly coupled device potentially due to the angular average effect in our TAM (the time-resolved system is not angle resolved). In general, by varying the coupling strength, we have also observed the new spectral feature in the TA spectra. Therefore, we can safely identify the new spectral feature as a signature of the formation of UP state in the strongly coupled device. However, the LP state, which should appear at ≈617.5 nm, is absent in our TA measurements. We hypothesize that the disappearance of the LP state is due to the enhanced photoinduced absorption (PA) band in our strongly coupled device, which is also indicated in Figure 4a. In other words, the bleaching signal of the LP state is hidden by the enhanced PA band. Since in the strong coupling regime, the wavefunctions of the hybridized states extend and become delocalized, and hence, the interactions between excitons or polaritons become notable, which may lead to an enhanced PA signal.

Another intriguing topic pertaining to strong coupling is the intrinsic lifetime of the exciton–polaritons. Normally, the dynamics of an exciton–polariton state lie in the Markovian regime,[90,99] where the decay trend is typically dominated by its fastest component (i.e., the cavity photon lifetime or bare exciton lifetime). However, recent reports have indicated the existence of trap states,[100] a phonon bottleneck effect,[101] and highly sensitive plasmonic nanostructures,[102] which can greatly modify the lifetime of these hybrid states. Therefore, it is suggested that the lifetime of a hybrid state is sensitively and strongly dependent on the specific system conditions,[103] such as the magnitude of the Rabi splitting, the active material and the type of optical resonator used. In Figure 4d, we compare the kinetics of the UP state in the WS_2-PhC device and the uncoupled exciton state in bare WS_2. Clearly, the lifetime of the UP state is only slightly shorter than that of the uncoupled exciton state. Considering that the Rabi splitting of our device is only slightly larger than the thermal energy $k_bT \simeq 25$ meV at room temperature, the Markovian approximation is applicable here. Thus, it is reasonable to attribute the quicker decay of the hybrid state to the additional damping channel (i.e., extra loss from the PhC) in the strongly coupled device. Nevertheless, to fully reveal the nature of this unique phenomenon, extensive further experimental and theoretical studies will be required.

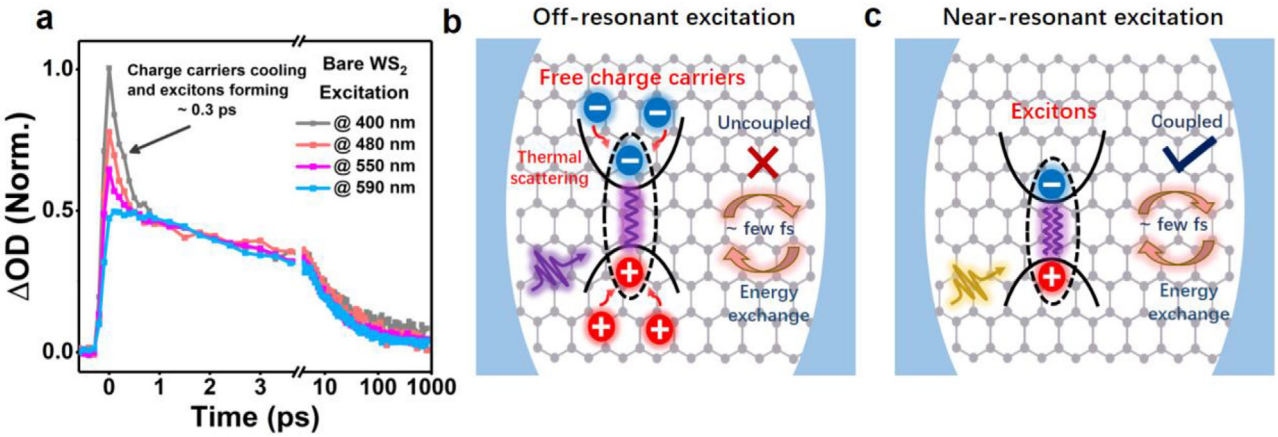

Figure 5. a) Dynamics of the A exciton bleaching (611.4 nm) of ML WS_2 under photoexcitation at wavelengths of 400, 480, 550, and 590 nm. All curves are normalized to the value at 2 ps for comparison. The black arrow indicates the sub-picosecond decay corresponding to the cooling of free charge carriers and the formation of excitons. Schematic cartoons of the interaction mechanisms in the WS_2-PhC polariton device under b) off-resonant excitation and c) near-resonant excitation, showing that the Coulomb interactions of the excitons in the ML WS_2 are efficiently screened under off-resonant excitation due to the presence of long-lived free charge carriers and nonequilibrium phonon scattering processes. In turn, the formation of a strongly coupled exciton–polariton state is also affected.

3.3. The Influence of Nonequilibrium Coulombic Screening to Strong Coupling

An equally significant question here is why the newly identified spectral signature of strong coupling can be detected in the TA spectrum only under near-resonant excitation. In fact, previous works[90] have asserted that the observed TA spectra and dynamics of strongly coupled devices are strongly affected by the thermal effect of the optical resonators under off-resonant excitation. For instance, in the case of surface plasmon polaritons (SPPs) structure, the hot electron distribution will affect their absorption properties.[100,101] However, considering that our strongly coupled device involves only interactions between the A excitons in the ML WS_2 and the guided modes of the PhC slab (instead of an SPP mode) and that the bare PhC contribute no TA signal, it can be predicted that our hybrid device should be free of any thermal effect from the optical resonator, that is, the 1D grating PhC here. Therefore, another physical explanation should be considered in this case. Since a thermal effect from the PhC is excluded, it is natural to investigate whether there is any difference in the carrier relaxation of the ML WS_2 under different excitation wavelengths. **Figure 5**a presents the relaxation of the A exciton state in the bare WS_2 under selected excitation wavelengths. It can be seen from this figure that there exists a sub-picosecond decay process (≈0.3 ps) that becomes more prominent at higher excitation energies. This fast decay component is attributed to the nonequilibrium process in which free charge carriers cool down and then form excitons, according to previous studies.[104–106] Thus, we can preliminarily speculate that the major difference between the cases of off-resonant and near-resonant excitation lies in the initially injected carrier species. More precisely, these species are either free charge carriers with excess energy (under off-resonant excitation) or excitons (under near-resonant excitation). However, a more in-depth study[107] has recently investigated the carrier dynamics of ML TMDs under nonresonant excitation using optical pump and mid-infrared probe spectroscopy (intraband response) and found that a significant fraction of free charge carriers are still present as free plasma on comparatively long time scales (i.e., they do not exist only within the sub-picosecond decay period), indicating a long-lived nonequilibrium state of the photoexcited electron–hole system under nonresonant optical excitation conditions. Moreover, this fast initial carrier relaxation could convert electronic excitation into phononic excitation, which can also lead to nonequilibrium phonon populations as well as a high effective carrier temperature in ML WS_2 and, potentially, to a mixture of excitons and unbound electron–hole pairs. Notably, these nonequilibrium phonon populations will last for time scales on the order of 100 ps, until they transfer heat to the underlying substrate, according to a previous report.[86] Based on these considerations, the key distinction between off-resonant and near-resonant excitation can be summarized as follows: under off-resonant excitation, the photoexcited carrier system that forms is a long-lived nonequilibrium mixed state of excitons and free charge carriers, while for near-resonant excitation, it is nearly a pure exciton system.

In summary, the complete physics picture of strong coupling developed in this study can be described as follows. The optically active excitons in the ML WS_2 emit photons into the PhC, and the PhC confine the photons in the vicinity of the ML WS_2. Next, the emitted photons can be reabsorbed by the excitons and re-emitted. This energy exchange process occurs on a time scale of approximately tens of femtoseconds[108] and will repeat, resulting in the occurrence of a strong coupling effect. It is worth noting that once the oscillator strength of the excitons is altered, this coherent energy exchange process will be blocked, hence affecting the formation of a strongly coupled hybrid state.[80,81] As shown in Figure 5b, under off-resonant excitation, the ultrafast laser pulse injects free charge carriers with considerable excess energy into the ML WS_2. The relaxation of this excess energy requires many thermal scattering processes, which can result in nonequilibrium carrier and phonon distributions in the system.[107] The presence of both long-lived free charge carriers and nonequilibrium

phonon populations can modify the Coulomb interactions of the excitons (reduction in oscillator strength) in the ML WS_2,[84–86] thus leading to the absence of a strong coupling effect.[109] By contrast, for the case of near-resonant excitation depicted in Figure 5c, the directly injected excitons are unaffected by thermal scattering processes and maintain their intrinsic characteristics, such as giant oscillator strength and large binding energy. These properties guarantee the strong coupling between the excitons of the ML WS_2 and the guided Bloch modes in the PhC. To further validate our conjecture, we carried out more TAM measurements at selected excitation wavelengths of 570 and 580 nm in Figure S9, Supporting Information. Notably, the UP state in TA spectra is found to be relatively weakened at 570 nm excitation condition. Here, we speculate the reason for this weakened UP state is that the photoinduced Coulombic screening effect starts to become predominant at 570 nm exciton since the energy difference between the 570 nm excitation and A exciton is about 146 meV, which is larger than energy difference between the 1s and 2s state of A exciton (≈140 meV). According to ref. [85], a fast decay feature emerges when the energy difference between excitation and A exciton is larger than energy difference between the 1s and 2s states of A exciton, and here we regard the occurrence of this fast decay feature as a starting point of photoinduced Coulombic screening effect. For 580 nm excitation, the energy difference between the excitation and A exciton is around 108 meV (<140 meV), which means the photoinduced Coulombic screening effect might be very weak under 580 nm excitation condition and hence the UP band in TA spectra is obvious. Our findings indicate that the ultrafast response of strongly coupled TMD-based polariton devices can be highly sensitive to nonequilibrium changes in the Coulombic screening in TMDs, which may be very helpful for achieving the active tunability of light–matter interactions and provide a new avenue toward the design of coherent light-control devices.

4. Conclusions

In conclusion, we have successfully established a simple strongly coupled WS_2-PhC device by taking advantage of the delocalized nature of guided Bloch modes in PhC, revealing a Rabi splitting of 40.2 meV and coherent hybrid polariton states with large spatial coherence length. Moreover, we have carried out an in-depth investigation on the transient dynamics of this strongly coupled WS_2-PhC device. Our experimental results reveal that a newly formed spectral feature is found in the TA spectrum under near-resonant excitation, which has been verified to correspond to the upper band of the hybrid exciton–polariton state. Furthermore, the underlying mechanism of the emergence of this intriguing spectral feature has been explored by comparing the ultrafast response of the strongly coupled WS_2-PhC device with that of bare WS_2 under excitation at different wavelengths, from off resonance to near resonance, showing that the nonequilibrium change in Coulombic screening induced by nonresonant photoexcitation has an enormous impact on the formation of the hybrid exciton–polariton state. Our work not only provides a fundamental understanding of the photophysics of strongly coupled devices based on TMDs but also shows excellent potential for the implementation of coherent devices.

5. Experimental Section

Angle-Resolved Reflectance and Photoluminescence Measurements: A home-made angle-resolved momentum–space imaging spectroscopy system was built using an Olympus microscope (IX73). The sample was irradiated by incident light from a tungsten lamp focused by an objective (40X magnitude, NA = 0.95). Using a series of convex lenses, the back focal plane of the same objective was imaged onto the entrance slit of an imaging spectrometer. Thus, the light reflected from the sample at a given angle corresponded to a single position on the entrance slit. This angle-resolved information or momentum–space information was imaged with a charge-coupled device (CCD; PIXIS 400) after the spectrometer (Princeton Instruments IsoPlane-320). A polarizer in the focal plane was used for polarization selection. The angle-resolved reflection ($R = I_S/I_{W/O}$) and extinction (Ext = 1 − R) spectra of the sample by normalizing the reflected light from the sample (I_S) with respect to the light reflected from a spot without sample ($I_{W/O}$) were obtained. High levels of extinction arose due to the excitation of the resonant modes of the structure. In the band structure measurement, one axis of the 2D CCD was used to resolve the angle of the reflected light, while the other axis was used to resolve the wavelength. The PL measurements were performed at room temperature. A continuous-wave solid-state laser was used to excite the ML WS_2 at a wavelength of 532 nm (with a maximum peak power of 50 mw), and the laser was focused by the same 40× objective onto the sample. The photoemission was analyzed with an angular resolution of 0.3° by the angle-resolved spectroscopy system.

Transient Absorption Microscopy Measurements: The ultrafast TA spectra of the strongly coupled WS_2-PhC device and the bare WS_2 area were measured via femtosecond pump–probe spectroscopy at room temperature. In the experimental setup, a Ti-sapphire laser system (Spectra-Physics) provided pulses centered at 800 nm with a pulse width of 65 fs and a repetition rate of 1 kHz. First, the output femtosecond pulse was divided into two distinct beams. The stronger beam (90%) was sent to an optical parametric amplifier (TOPAS, Coherent) to generate tunable excitation pulses, and the other beam (10%) was focused onto a sapphire crystal to generate a white-light continuum beam to serve as the probe beam. Then, the white-light continuum beam, spanning the spectral range from 450 to 750 nm, was collimated using a reflective parabolic mirror to minimize temporal chirp. Finally, the cross-polarized pump and probe beams were sent collinearly to a reflective objective (Thorlabs, LMM-40X-P01; the incident probe beam covered an angular range from 9.1° to 19.7°) to be focused on the sample to a laser spot size of ≈5 μm (the reflective objective introduced no temporal chirp in either the pump or probe beam). The delay between the pump and probe beam was acquired using a precise delay line in the optical path of the probe beam. The variation in the optical density (ΔOD) of the probe beam between the pump case and the no-pump case was recorded using a monochromator followed by a Si detector. Specifically, the variation in the optical density is defined as $\Delta OD = -\log(R_{probe}^{pump}/R_{probe}^{no\ pump})$, where R_{probe}^{pump} represents the reflection of the probe beam affected by the pre-existing pump beam, whereas $R_{probe}^{no\ pump}$ represents the reflectivity of the probe under conditions far from the pump excitation.

Supporting Information

Supporting Information is available from the Wiley Online Library or from the author.

Acknowledgements

Y.T. and Y.Z. contributed equally to this work. The authors are grateful for the financial support from the National Natural Science Foundation (NSF) of China (11802339, 11805276, 61805282, 61801498, 11804387, 11774063, and 11727811), the 973 Program and the China National Key Basic Research Program (Program Nos. 2015CB659400 and

2016YFA0302000), the Scientific Research Foundation of the National University of Defense Technology (ZK16-03-59, ZK18-01-03, ZK18-03-36, and ZK18-03-22), the NSF of Hunan Province (2016JJ1021), the Open Director Fund of the State Key Laboratory of Pulsed Power Laser Technology (SKL2018ZR05), the Open Research Fund of Hunan Provincial Key Laboratory of High Energy Technology (GNJGJS03), the Opening Foundation of the State Key Laboratory of Laser Interaction with Matter (SKLLIM1702); a Youth Talent Lifting Project (17-JCJQ-QT-004), and the Science and Technology Commission of Shanghai Municipality (Grant Nos. 17ZR1442300 and 17142200100)

Conflict of Interest

The authors declare no conflict of interest.

Keywords

Coulombic screening, photonic crystals, Rabi splitting, strong coupling, transient absorption microscopy, transition metal dichalcogenides

Received: November 30, 2019
Revised: January 23, 2020
Published online: March 5, 2020

[1] S. Wu, S. Buckley, J. R. Schaibley, L. Feng, J. Yan, D. G. Mandrus, F. Hatami, W. Yao, J. Vučković, A. Majumdar, X. Xu, *Nature* **2015**, *520*, 69.
[2] W. Du, S. Zhang, Q. Zhang, X. Liu, *Adv. Mater.* **2018**, 1804894.
[3] A. Krasnok, S. Lepeshov, A. Alú, *Opt. Express* **2018**, *26*, 15972.
[4] F. Hu, Z. Fei, *Adv. Opt. Mater.* **2019**, 1901003.
[5] C. Zhang, H. Ouyang, R. Miao, Y. Sui, H. Hao, Y. Tang, J. You, X. Zheng, Z. Xu, X. Cheng, T. Jiang, *Adv. Opt. Mater.* **2019**, *7*, 1900631.
[6] R. Miao, Y. Hu, H. Ouyang, Y. Tang, C. Zhang, J. You, X. Zheng, Z. Xu, X. Cheng, T. Jiang, *Nanoscale* **2019**, *11*, 14598.
[7] J. T. Hugall, A. Singh, N. F. van Hulst, *ACS Photonics* **2018**, *5*, 43.
[8] P. Vasa, C. Lienau, *ACS Photonics* **2018**, *5*, 2.
[9] D. G. Baranov, M. Wersäll, J. Cuadra, T. J. Antosiewicz, T. Shegai, *ACS Photonics* **2018**, *5*, 24.
[10] X. Yu, Y. Yuan, J. Xu, K.-T. Yong, J. Qu, J. Song, *Laser Photonics Rev.* **2019**, *13*, 1800219.
[11] D. S. Dovzhenko, S. V. Ryabchuk, Y. P. Rakovich, I. R. Nabiev, *Nanoscale* **2018**, *10*, 3589.
[12] M. Hertzog, M. Wang, J. Mony, K. Börjesson, *Chem. Soc. Rev.* **2019**, *48*, 937.
[13] H. Shan, Y. Yu, X. Wang, Y. Luo, S. Zu, B. Du, T. Han, B. Li, Y. Li, J. Wu, F. Lin, K. Shi, B. K. Tay, Z. Liu, X. Zhu, Z. Fang, *Light: Sci. Appl.* **2019**, *8*, 9.
[14] W. Du, J. Zhao, W. Zhao, S. Zhang, H. Xu, Q. Xiong, *ACS Photonics* **2019**, *6*, 11.
[15] X. Gan, Y. Gao, K. F. Mak, X. Yao, R.-J. Shiue, A. van der Zande, M. E. Trusheim, F. Hatami, T. F. Heinz, J. Hone, D. Englund, *Appl. Phys. Lett.* **2013**, *103*, 181119.
[16] S. Wu, S. Buckley, A. M. Jones, J. S. Ross, N. J. Ghimire, J. Yan, D. G. Mandrus, W. Yao, F. Hatami, J. Vučković, A. Majumdar, X. Xu, *2D Mater.* **2014**, *1*, 011001.
[17] X. Zhang, S. Choi, D. Wang, C. H. Naylor, A. T. C. Johnson, E. Cubukcu, *Nano Lett.* **2017**, *17*, 6715.
[18] C.-H. Liu, G. Clark, T. Fryett, S. Wu, J. Zheng, F. Hatami, X. Xu, A. Majumdar, *Nano Lett.* **2017**, *17*, 200.
[19] S. Dufferwiel, S. Schwarz, F. Withers, A. A. P. Trichet, F. Li, M. Sich, O. Del Pozo-Zamudio, C. Clark, A. Nalitov, D. D. Solnyshkov, G. Malpuech, K. S. Novoselov, J. M. Smith, M. S. Skolnick, D. N. Krizhanovskii, A. I. Tartakovskii, *Nat. Commun.* **2015**, *6*, 8579.
[20] D. N. Basov, M. M. Fogler, F. J. Garcia de Abajo, *Science* **2016**, *354*, aag1992.
[21] T. Low, A. Chaves, J. D. Caldwell, A. Kumar, N. X. Fang, P. Avouris, T. F. Heinz, F. Guinea, L. Martin-Moreno, F. Koppens, *Nat. Mater.* **2017**, *16*, 182.
[22] T. K. Hakala, J. J. Toppari, A. Kuzyk, M. Pettersson, H. Tikkanen, H. Kunttu, P. Törmä, *Phys. Rev. Lett.* **2009**, *103*, 053602.
[23] A. González-Tudela, P. A. Huidobro, L. Martín-Moreno, C. Tejedor, F. J. García-Vidal, *Phys. Rev. Lett.* **2013**, *110*, 126801.
[24] L. Shi, X. Yuan, Y. Zhang, T. Hakala, S. Yin, D. Han, X. Zhu, B. Zhang, X. Liu, P. Törmä, W. Lu, J. Zi, *Laser Photonics Rev.* **2014**, *8*, 717.
[25] A. I. Väkeväinen, R. J. Moerland, H. T. Rekola, A.-P. Eskelinen, J.-P. Martikainen, D.-H. Kim, P. Törmä, *Nano Lett.* **2014**, *14*, 1721.
[26] L. Shi, T. K. Hakala, H. T. Rekola, J.-P. Martikainen, R. J. Moerland, P. Törmä, *Phys. Rev. Lett.* **2014**, *112*, 153002.
[27] P. Törmä, W. L. Barnes, *Rep. Prog. Phys.* **2015**, *78*, 013901.
[28] N. Lundt, S. Klembt, E. Cherotchenko, S. Betzold, O. Iff, A. V. Nalitov, M. Klaas, C. P. Dietrich, A. V. Kavokin, S. Höfling, C. Schneider, *Nat. Commun.* **2016**, *7*, 13328.
[29] A. Tsargorodska, M. L. Cartron, C. Vasilev, G. Kodali, O. A. Mass, J. J. Baumberg, P. L. Dutton, C. N. Hunter, P. Törmä, G. J. Leggett, *Nano Lett.* **2016**, *16*, 6850.
[30] E. Cao, W. Lin, M. Sun, W. Liang, Y. Song, *Nanophotonics* **2018**, *7*, 145.
[31] L. Novotny, *Am. J. Phys.* **2010**, *78*, 1199.
[32] M. Waldherr, N. Lundt, M. Klaas, S. Betzold, M. Wurdack, V. Baumann, E. Estrecho, A. Nalitov, E. Cherotchenko, H. Cai, E. A. Ostrovskaya, A. V. Kavokin, S. Tongay, S. Klembt, S. Höfling, C. Schneider, *Nat. Commun.* **2018**, *9*, 3286.
[33] E. Orgiu, J. George, J. A. Hutchison, E. Devaux, J. F. Dayen, B. Doudin, F. Stellacci, C. Genet, J. Schachenmayer, C. Genes, G. Pupillo, P. Samorì, T. W. Ebbesen, *Nat. Mater.* **2015**, *14*, 1123.
[34] J. Feist, F. J. Garcia-Vidal, *Phys. Rev. Lett.* **2015**, *114*, 196402.
[35] G. G. Rozenman, K. Akulov, A. Golombek, T. Schwartz, *ACS Photonics* **2018**, *5*, 105.
[36] F. J. Garcia-Vidal, J. Feist, *Science* **2017**, *357*, 1357.
[37] T. Schwartz, J. A. Hutchison, C. Genet, T. W. Ebbesen, *Phys. Rev. Lett.* **2011**, *106*, 196405.
[38] M. Ramezani, A. Halpin, A. I. Fernández-Domínguez, J. Feist, S. R.-K. Rodriguez, F. J. Garcia-Vidal, J. G. Rivas, *Optica* **2017**, *4*, 31.
[39] T. J. S. Evans, A. Schlaus, Y. Fu, X. Zhong, T. L. Atallah, M. S. Spencer, L. E. Brus, S. Jin, X.-Y. Zhu, *Adv. Opt. Mater.* **2018**, *6*, 1700982.
[40] R. Su, C. Diederichs, J. Wang, T. C. H. Liew, J. Zhao, S. Liu, W. Xu, Z. Chen, Q. Xiong, *Nano Lett.* **2017**, *17*, 3982.
[41] W. Du, S. Zhang, J. Shi, J. Chen, Z. Wu, Y. Mi, Z. Liu, Y. Li, X. Sui, R. Wang, X. Qiu, T. Wu, Y. Xiao, Q. Zhang, X. Liu, *ACS Photonics* **2018**, *5*, 2051.
[42] J. Wang, P. Da, Z. Zhang, S. Luo, L. Liao, Z. Sun, X. Shen, S. Wu, G. Zheng, Z. Chen, *Nanoscale* **2018**, *10*, 10371.
[43] B. Kolaric, B. Maes, K. Clays, T. Durt, Y. Caudano, *Adv. Quantum Technol.* **2018**, *1*, 1800001.
[44] K. F. Mak, C. Lee, J. Hone, J. Shan, T. F. Heinz, *Phys. Rev. Lett.* **2010**, *105*, 136805.
[45] Q. H. Wang, K. Kalantar-Zadeh, A. Kis, J. N. Coleman, M. S. Strano, *Nat. Nanotechnol.* **2012**, *7*, 699.
[46] F. Xia, H. Wang, D. Xiao, M. Dubey, A. Ramasubramaniam, *Nat. Photonics* **2014**, *8*, 899.
[47] K. F. Mak, J. Shan, *Nat. Photonics* **2016**, *10*, 216.
[48] T. Cao, G. Wang, W. Han, H. Ye, C. Zhu, J. Shi, Q. Niu, P. Tan, E. Wang, B. Liu, J. Feng, *Nat. Commun.* **2012**, *3*, 887.

[49] K. F. Mak, K. He, J. Shan, T. F. Heinz, *Nat. Nanotechnol.* **2012**, *7*, 494.
[50] G. Sallen, L. Bouet, X. Marie, G. Wang, C. R. Zhu, W. P. Han, Y. Lu, P. H. Tan, T. Amand, B. L. Liu, B. Urbaszek, *Phys. Rev. B* **2012**, *86*, 081301.
[51] D. Xiao, G.-B. Liu, W. Feng, X. Xu, W. Yao, *Phys. Rev. Lett.* **2012**, *108*, 196802.
[52] H. Zeng, J. Dai, W. Yao, D. Xiao, X. Cui, *Nat. Nanotechnol.* **2012**, *7*, 490.
[53] A. M. Jones, H. Yu, N. J. Ghimire, S. Wu, G. Aivazian, J. S. Ross, B. Zhao, J. Yan, D. G. Mandrus, D. Xiao, W. Yao, X. Xu, *Nat. Nanotechnol.* **2013**, *8*, 634.
[54] X. Xu, W. Yao, D. Xiao, T. F. Heinz, *Nat. Phys.* **2014**, *10*, 343.
[55] C. Schneider, M. M. Glazov, T. Korn, S. Höfling, B. Urbaszek, *Nat. Commun.* **2018**, *9*, 2695.
[56] E. Eizner, O. Avayu, R. Ditcovski, T. Ellenbogen, *Nano Lett.* **2015**, *15*, 6215.
[57] Q. Shang, S. Zhang, Z. Liu, J. Chen, P. Yang, C. Li, W. Li, Y. Zhang, Q. Xiong, X. Liu, Q. Zhang, *Nano Lett.* **2018**, *18*, 3335.
[58] S. Zhang, Q. Shang, W. Du, J. Shi, Z. Wu, Y. Mi, J. Chen, F. Liu, Y. Li, M. Liu, Q. Zhang, X. Liu, *Adv. Opt. Mater.* **2018**, *6*, 1701032.
[59] X. Liu, T. Galfsky, Z. Sun, F. Xia, E. Lin, Y.-H. Lee, S. Kéna-Cohen, V. M. Menon, *Nat. Photonics* **2015**, *9*, 30.
[60] X. Liu, W. Bao, Q. Li, C. Ropp, Y. Wang, X. Zhang, *Phys. Rev. Lett.* **2017**, *119*, 027403.
[61] M.-E. Kleemann, R. Chikkaraddy, E. M. Alexeev, D. Kos, C. Carnegie, W. Deacon, A. C. de Pury, C. Große, B. de Nijs, J. Mertens, A. I. Tartakovskii, J. J. Baumberg, *Nat. Commun.* **2017**, *8*, 1296.
[62] J. Wen, H. Wang, W. Wang, Z. Deng, C. Zhuang, Y. Zhang, F. Liu, J. She, J. Chen, H. Chen, S. Deng, N. Xu, *Nano Lett.* **2017**, *17*, 4689.
[63] X. Han, K. Wang, X. Xing, M. Wang, P. Lu, *ACS Photonics* **2018**, *5*, 3970.
[64] J. Cuadra, D. G. Baranov, M. Wersäll, R. Verre, T. J. Antosiewicz, T. Shegai, *Nano Lett.* **2018**, *18*, 1777.
[65] M. Stührenberg, B. Munkhbat, D. G. Baranov, J. Cuadra, A. B. Yankovich, T. J. Antosiewicz, E. Olsson, T. Shegai, *Nano Lett.* **2018**, *18*, 5938.
[66] J. Sun, H. Hu, D. Zheng, D. Zhang, Q. Deng, S. Zhang, H. Xu, *ACS Nano* **2018**, *12*, 10393.
[67] W. Liu, B. Lee, C. H. Naylor, H.-S. Ee, J. Park, A. T. C. Johnson, R. Agarwal, *Nano Lett.* **2016**, *16*, 1262.
[68] S. Wang, S. Li, T. Chervy, A. Shalabney, S. Azzini, E. Orgiu, J. A. Hutchison, C. Genet, P. Samorì, T. W. Ebbesen, *Nano Lett.* **2016**, *16*, 4368.
[69] B. Lee, W. Liu, C. H. Naylor, J. Park, S. C. Malek, J. S. Berger, A. T. C. Johnson, R. Agarwal, *Nano Lett.* **2017**, *17*, 4541.
[70] S. Zhang, H. Zhang, T. Xu, W. Wang, Y. Zhu, D. Li, Z. Zhang, J. Yi, W. Wang, *Phys. Rev. B* **2018**, *97*, 235401.
[71] S. Wang, Q. Le-Van, F. Vaianella, B. Maes, S. E. Barker, R. H. Godiksen, A. G. Curto, J. G. Rivas, *ACS Photonics* **2019**, *6*, 286.
[72] X. Chen, H. Wang, N.-S. Xu, H. Chen, S. Deng, *Appl. Mater. Today* **2019**, *15*, 145.
[73] S. Dufferwiel, T. P. Lyons, D. D. Solnyshkov, A. A. P. Trichet, F. Withers, S. Schwarz, G. Malpuech, J. M. Smith, K. S. Novoselov, M. S. Skolnick, D. N. Krizhanovskii, A. I. Tartakovskii, *Nat. Photonics* **2017**, *11*, 497.
[74] Z. Sun, J. Gu, A. Ghazaryan, Z. Shotan, C. R. Considine, M. Dollar, B. Chakraborty, X. Liu, P. Ghaemi, S. Kéna-Cohen, V. M. Menon, *Nat. Photonics* **2017**, *11*, 491.
[75] Y.-J. Chen, J. D. Cain, T. K. Stanev, V. P. Dravid, N. P. Stern, *Nat. Photonics* **2017**, *11*, 431.
[76] N. Lundt, S. Stoll, P. Nagler, A. Nalitov, S. Klembt, S. Betzold, J. Goddard, E. Frieling, A. V. Kavokin, C. Schüller, T. Korn, S. Höfling, C. Schneider, *Phys. Rev. B* **2017**, *96*, 241403.
[77] J. Gu, B. Chakraborty, M. Khatoniar, V. M. Menon, *Nat. Nanotechnol.* **2019**, *14*, 1024.
[78] L. Zhang, R. Gogna, W. Burg, E. Tutuc, H. Deng, *Nat. Commun.* **2018**, *9*, 713.
[79] B. Višić, L. Yadgarov, E. A. A. Pogna, S. Dal Conte, V. Vega-Mayoral, D. Vella, R. Tenne, G. Cerullo, C. Gadermaier, *Phys. Rev. Res.* **2019**, *1*, 033046.
[80] B. Chakraborty, J. Gu, Z. Sun, M. Khatoniar, R. Bushati, A. L. Boehmke, R. Koots, V. M. Menon, *Nano Lett.* **2018**, *18*, 6455.
[81] H. A. Fernandez, F. Withers, S. Russo, W. L. Barnes, *Adv. Opt. Mater.* *7*, **2019**, 1900484.
[82] A. Chernikov, T. C. Berkelbach, H. M. Hill, A. Rigosi, Y. Li, O. B. Aslan, D. R. Reichman, M. S. Hybertsen, T. F. Heinz, *Phys. Rev. Lett.* **2014**, *113*, 076802.
[83] A. Chernikov, A. M. van der Zande, H. M. Hill, A. F. Rigosi, A. Velauthapillai, J. Hone, T. F. Heinz, *Phys. Rev. Lett.* **2015**, *115*, 126802.
[84] E. A. A. Pogna, M. Marsili, D. De Fazio, S. Dal Conte, C. Manzoni, D. Sangalli, D. Yoon, A. Lombardo, A. C. Ferrari, A. Marini, G. Cerullo, D. Prezzi, *ACS Nano* **2016**, *10*, 1182.
[85] P. D. Cunningham, A. T. Hanbicki, K. M. McCreary, B. T. Jonker, *ACS Nano* **2017**, *11*, 12601.
[86] C. Ruppert, A. Chernikov, H. M. Hill, A. F. Rigosi, T. F. Heinz, *Nano Lett.* **2017**, *17*, 644.
[87] H. Li, X. Zheng, Y. Liu, Z. Zhang, T. Jiang, *Nanoscale* **2018**, *10*, 1650.
[88] Y. Tang, T. Jiang, T. Zhou, H. Hao, K. Wei, H. Li, J. You, Z. Wang, X. Zheng, Z. Xu, X. Cheng, *Nanotechnology* **2019**, *30*, 325702.
[89] R. Miao, Y. Zhang, Y. Tang, J. You, Y. Zhang, L. Shi, T. Jiang, *Opt. Lett.* **2018**, *43*, 6093.
[90] H. Wang, H. Wang, H. Sun, A. Cerea, A. Toma, F. Angelis, X. Jin, L. Razzari, D. Cojoc, D. Catone, F. Huang, R. P. Zaccaria, *Adv. Funct. Mater.* **2018**, *28*, 1801761.
[91] K. Wei, T. Jiang, Z. Xu, J. Zhou, J. You, Y. Tang, H. Li, R. Chen, X. Zheng, S. Wang, K. Yin, Z. Wang, J. Wang, X. Cheng, *Laser Photonics Rev.* **2018**, *12*, 1800128.
[92] K. Wei, X. Zheng, X. Cheng, C. Shen, T. Jiang, *Adv. Opt. Mater.* **2016**, *4*, 1993.
[93] T. Jiang, R. Chen, X. Zheng, Z. Xu, Y. Tang, *Opt. Express* **2018**, *26*, 859.
[94] H. Hao, Z. Xu, T. Jiang, K. Wei, H. Li, X. Zheng, K. Yin, J. You, C. Shen, X. Cheng, *Opt. Express* **2018**, *26*, 15867.
[95] E. J. Sie, C. H. Lui, Y.-H. Lee, J. Kong, N. Gedik, *Nano Lett.* **2016**, *16*, 7421.
[96] J. Pei, J. Yang, T. Yildirim, H. Zhang, Y. Lu, *Adv. Mater.* **2019**, *31*, 1706945.
[97] P. D. Cunningham, K. M. McCreary, B. T. Jonker, *J. Phys. Chem. Lett.* **2016**, *7*, 5242.
[98] L. Yuan, T. Wang, T. Zhu, M. Zhou, L. Huang, *J. Phys. Chem. Lett.* **2017**, *8*, 3371.
[99] A. Canaguier-Durand, C. Genet, A. Lambrecht, T. W. Ebbesen, S. Reynaud, *Eur. Phys. J. D* **2015**, *69*, 24.
[100] H. Wang, H.-Y. Wang, A. Bozzola, A. Toma, S. Panaro, W. Raja, A. Alabastri, L. Wang, Q.-D. Chen, H.-L. Xu, F. De Angelis, H.-B. Sun, R. P. Zaccaria, *Adv. Funct. Mater.* **2016**, *26*, 6198.
[101] H. Wang, H.-Y. Wang, A. Toma, T. Yano, Q.-D. Chen, H.-L. Xu, H.-B. Sun, R. P. Zaccaria, *J. Phys. Chem. Lett.* **2016**, *7*, 4648.
[102] E. Eizner, K. Akulov, T. Schwartz, T. Ellenbogen, *Nano Lett.* **2017**, *17*, 7675.
[103] H. Wang, H.-Y. Wang, Q.-D. Chen, H.-L. Xu, H.-B. Sun, F. Huang, W. Raja, A. Toma, R. P. Zaccaria, *Laser Photonics Rev.* **2018**, *12*, 1700176.
[104] F. Ceballos, Q. Cui, M. Z. Bellus, H. Zhao, *Nanoscale* **2016**, *8*, 11681.

[105] P. D. Cunningham, K. M. McCreary, A. T. Hanbicki, M. Currie, B. T. Jonker, L. M. Hayden, *J. Phys. Chem. C* **2016**, *120*, 5819.
[106] Z. Nie, R. Long, L. Sun, C.-C. Huang, J. Zhang, Q. Xiong, D. W. Hewak, Z. Shen, O. V. Prezhdo, Z.-H. Loh, *ACS Nano* **2014**, *8*, 10931.
[107] P. Steinleitner, P. Merkl, P. Nagler, J. Mornhinweg, C. Schüller, T. Korn, A. Chernikov, R. Huber, *Nano Lett.* **2017**, *17*, 1455.
[108] P. Vasa, W. Wang, R. Pomraenke, M. Lammers, M. Maiuri, C. Manzoni, G. Cerullo, C. Lienau, *Nat. Photonics* **2013**, *7*, 128.
[109] J. Gu, L. Waldecker, D. Rhodes, A. Boehmke, A. Raja, R. Koots, J. C. Hone, T. F. Heinz, V. M. Menon, in *Conference on Lasers and Electro-Optics*, Optical Society Of America, Washington, DC **2019**, p. FW3M.5.